

# A study of dust properties in the inner sub-au region of the Herbig Ae star HD 169142 with VLTI/PIONIER $\star$

L. Chen<sup>1</sup>, Á. Kóspál<sup>1,2</sup>, P. Ábrahám<sup>1</sup>, A. Kreplin<sup>3</sup>, A. Matter<sup>4</sup>, and G. Weigelt<sup>5</sup>

<sup>1</sup> Konkoly Observatory, Research Centre for Astronomy and Earth Sciences, Hungarian Academy of Sciences, Konkoly Thege Miklós út 15-17, 1121 Budapest, Hungary  
email: lei.chen@csfk.mta.hu

<sup>2</sup> Max-Planck-Institut für Astronomie, Königstuhl 17, 69117 Heidelberg, Germany

<sup>3</sup> University of Exeter, Department of Physics and Astronomy, Stocker Road, Exeter, Devon EX4 4QL, UK

<sup>4</sup> Laboratoire Lagrange, Université Côte d'Azur, Observatoire de la Côte d'Azur, CNRS, Boulevard de l'Observatoire, CS 34229, 06304 Nice Cedex 4, France

<sup>5</sup> Max-Planck-Institut für Radioastronomie, Auf dem Hügel 69, 53121 Bonn, Germany

Preprint online version: May 5, 2021

## ABSTRACT

**Context.** An essential step to understanding protoplanetary evolution is the study of disks that contain gaps or inner holes. The pre-transitional disk around the Herbig star HD 169142 exhibits multi-gap disk structure, differentiated gas and dust distribution, planet candidates, and near-infrared fading in the past decades, which make it a valuable target for a case study of disk evolution.

**Aims.** Using near-infrared interferometric observations with VLTI/PIONIER, we aim to study the dust properties in the inner sub-au region of the disk in the years 2011-2013, when the object is already in its near-infrared faint state.

**Methods.** We first performed simple geometric modeling to characterize the size and shape of the NIR-emitting region. We then performed Monte-Carlo radiative transfer simulations on grids of models and compared the model predictions with the interferometric and photometric observations.

**Results.** We find that the observations are consistent with optically thin gray dust lying at  $R_{\text{in}} \sim 0.07$  au, passively heated to  $T \sim 1500$  K. Models with sub-micron optically thin dust are excluded because such dust will be heated to much higher temperatures at similar distance. The observations can also be reproduced with a model consisting of optically thick dust at  $R_{\text{in}} \sim 0.06$  au, but this model is plausible only if refractory dust species enduring  $\sim 2400$  K exist in the inner disk.

**Key words.** accretion: accretion disks - techniques: interferometric - protoplanetary disks - circumstellar matter - stars: pre-main sequence - stars: individual: HD169142

## 1. Introduction

An essential step to understanding protoplanetary evolution is the study of disks that contain gaps or inner holes. These objects are likely to be in a late evolutionary stage and are probably progenitors of debris disks. The existence of gaps and holes may be inferred from the spectral energy distribution (SED) in infrared (IR). Protoplanetary disks around Herbig Ae stars are classified into two groups depending on the shape of their SEDs (Meeus et al. 2001). While a group II object has roughly a power-law SED from near-infrared (NIR) to FIR, the SED of a group I object has an additional cold component at mid-infrared (MIR) or far-infrared (FIR) wavelengths. A recent explanation of the two types is that group I SEDs are caused by disk gaps, while group II objects typically have continuous disks (Maaskant et al. 2013). However, Menu et al. (2015) suggested that group II objects can have gaps that are narrow enough not to cause appreciable signatures in the SEDs. Gaps and inner holes have been directly detected with spatially resolved observations in a growing number of protoplanetary disks (e.g., Isella et al. 2016; van der Marel et al. 2013).

The Herbig Ae star HD 169142 exhibits a typical group I SED, with strong evidence for the presence of wide gap regions in its disk. With direct MIR imaging, Honda et al. (2012) found an inner cavity with a size of  $\sim 23$  au in the MIR image of the disk. However, the NIR excess indicates that hot dust still exists around the central star. Honda et al. (2012) therefore suggested that HD 169142 has a wide gap separating a hot inner disk from a colder outer disk, which would make this object “an excellent candidate to look for newly formed planets in the protoplanetary disk”. Polarimetric imaging in the NIR of the object (Quanz et al. 2013) not only confirmed the cavity inside  $\sim 20$  au, but also found a second gap at 40–70 au, just behind the inner rim of the outer disk. Recent NIR polarized imaging (Momose et al. 2015; Monnier et al. 2017) confirmed the double-gap disk structure. These discoveries show HD 169142 to be among the first objects in which multiple gaps have been found. A point-like IR source, possibly a brown dwarf or a forming planet, was found at  $\sim 23$  au from the central star, that is, just at the inner rim of the outer disk (Biller et al. 2014; Reggiani et al. 2014). With radio observations at 7 mm, Osorio et al. (2014) confirmed that the second gap is likely to be caused by a dip in surface density profile, and found a possible point source in this gap region. Very recently, imaging at 7 mm and 9 mm revealed another gap at  $\sim 85$  au (Macías et al. 2017). A decoupling of dust and gas components was found with the

$\star$  Based on observations collected at the European Organisation for Astronomical Research in the Southern Hemisphere under ESO programs 190.C-963 and 087.C-0709.

latest ALMA observation (Fedele et al. 2017). The dust continuum map exhibits similar gap regions as those in the NIR polarized light, indicating that, instead of a shadowing effect, the gap regions are indeed related to a dip in surface density profile of dust. However, the CO line intensity map indicates that gas components exist continuously in the gap regions.

Wagner et al. (2015) found a decrease of 45% in the NIR excess of HD 169142 over a timescale of not more than 10 yr, from a pre-2000 high state to a post-2000 low state. They interpreted the variability as caused by changes in the dust distribution of an optically thin inner component, while the optically thick core in their model remains constant during the period of NIR variability.

The multi-gap disk structure, differentiated gas and dust distribution, planet candidates, and the variation in the inner disk make HD 169142 a valuable target for a case study of disk evolution. However, spatially resolved observations of the inner disk, where the most rapid evolution is happening, are still rare. Recently, infrared interferometric observations of HD 169142 with VLTI/PIONIER, which for the first time resolved the sub- $a$ u scale inner disk, were reported in Lazareff et al. (2017), as part of a large survey project.

In this paper we present both refined geometric modeling of HD 169142 using a larger data set, and our Monte-Carlo radiative transfer modeling using RADMC3D<sup>1</sup>. Our study aims to constrain the dust properties of the inner disk. Because all the NIR interferometric observations used in this work were performed between the years 2011 and 2013, our study constrains the dust properties in this period alone when the object was already in its low state (Wagner et al. 2015).

In our study we adopt a distance of  $117 \pm 4$  pc, derived from the recently measured parallax of  $8.53 \pm 0.29$  mas for HD 169142 in Gaia DR1 (Gaia Collaboration et al. 2016). We note that a distance of  $d = 145$  pc was used in most of the previous studies (e.g., Honda et al. 2012; Wagner et al. 2015), but most of our results are scalable and physically unaltered when adopting either distance value.

## 2. Observations and data reduction

### 2.1. PIONIER Observations

HD 169142 was observed with the VLTI/PIONIER instrument on one night in 2011 (ESO program 087.C-0709) and three nights in 2013 (ESO program 190.C-963). PIONIER is a four-telescope beam combiner that works in the H band (Le Bouquin et al. 2011), providing spectrally dispersed visibilities and closure phases. The observations were conducted using several baseline configurations<sup>2</sup> of the 1.8 m auxiliary telescopes (ATs). Each observation was preceded and followed by the observation of a calibrator to characterize the instrumental transfer function. A complete observation log is presented in Table 1. The data were reduced with the PNDRS package as described in Le Bouquin et al. (2011). The reduced archival OIFITS files were retrieved from the Optical Interferometry Database (OiDB, Haubois et al. 2014).

Out of the seven interferometric observations, we analyzed the first six, and discarded the last one (2011d) because of its low data quality. The  $uv$ -coverage of the final data set is plotted in Fig. 1. The measured visibilities as function of wavelength are plotted in Fig. 4, and the band-averaged visibilities are plotted

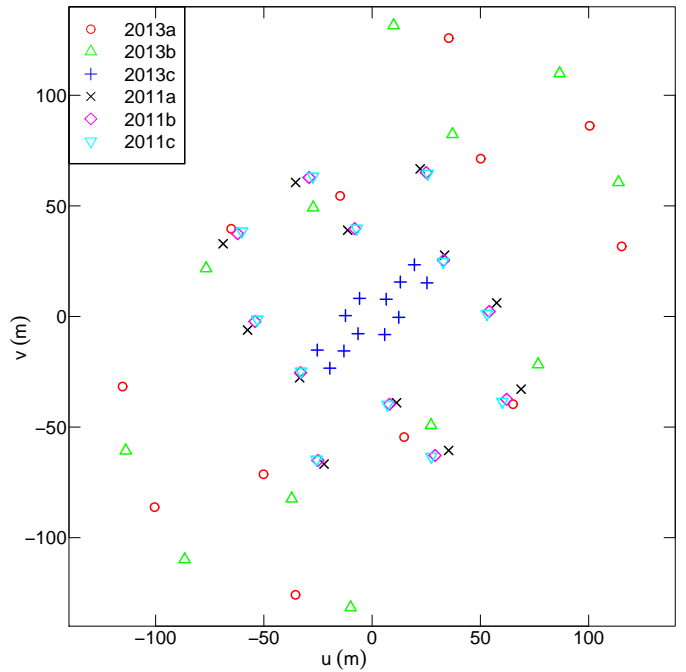


**Fig. 1.**  $uv$ -coverage of our interferometric observations.

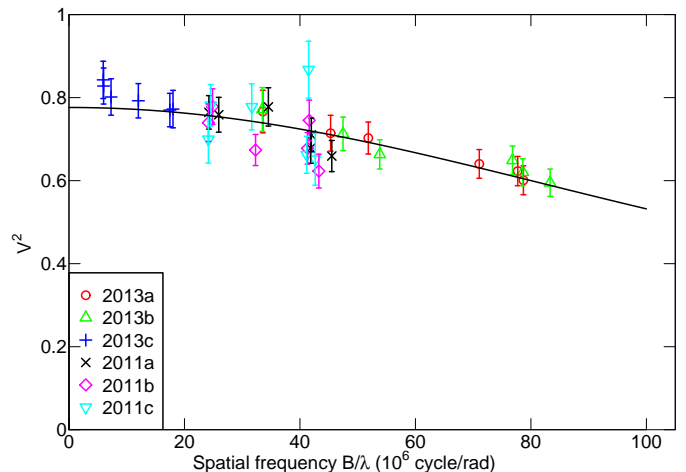


**Fig. 2.** Visibilities from the PIONIER observations of HD 169142, and our star-ring-halo model fitting.

in Fig. 2. The measured closure phases are not plotted because they are all close to zero. For the estimation of the uncertainty of the visibilities, we assumed a calibration error of 5%, and quadratically added it to the random error given by the reduction software.

### 2.2. The optical-NIR SED

For the interpretation of the interferometric data, complementary photometric data are essential. We adopted the photometric observations obtained in the UBVRIJHK bands with the Sutherland SAAO telescope (performed in 2014, Lazareff et al. 2017), the optical photometry collected in Wagner et al. (2015), and the observations with SpeX spectrograph on NASA's Infrared Telescope Facility (performed in 2013, Wagner et al. 2015). The compiled SED is shown in Fig. 3. Among the NIR photometric data, we adopted only those from epochs close to

<sup>1</sup> <http://www.ita.uni-heidelberg.de/~dullemond/software/radmc-3d/>

<sup>2</sup> <http://www.eso.org/sci/facilities/paranal/telescopes/vlti/configuration>

**Table 1.** Observation log of our VLTI/PIONIER observations of HD 169142. For each observation, the information on the six baselines are shown.  $B_p$  is the projected baseline length. PA is the position angle from north to east.

Data set	Night	Telescope configuration	$u$ (m)	$v$ (m)	$B_p$ (m)	PA ( $^{\circ}$ )
2013a	2013-06-04	A1-G1-J3-K0	-14.8	54.5	56.5	-15.2
			-50.2	-71.3	87.2	-144.9
			65.1	-39.6	76.2	121.3
			100.5	86.2	132.4	49.4
			-115.2	-31.7	119.5	-105.4
			35.4	125.8	130.7	15.7
2013b	2013-06-09	A1-G1-J3-K0	-37.1	-82.4	90.3	-155.7
			-113.8	-60.7	128.9	-118.1
			9.9	131.6	131.9	4.3
			76.7	-21.7	79.7	105.8
			86.6	109.9	139.9	38.2
			-27.2	49.2	56.2	-28.9
2013c	2013-07-03	A1-B2-C1-D0	-25.3	-15.2	29.5	-121.0
			12.3	-0.4	12.3	91.8
			-6.5	-7.8	10.1	-140.2
			-13.0	-15.6	20.3	-140.1
			5.8	-8.2	10.0	144.6
			-19.5	-23.4	30.5	-140.1
2011a	2011-06-05	D0-G1-H0-I1	68.8	-32.9	76.3	115.5
			22.2	66.7	70.3	18.4
			33.5	27.7	43.5	50.4
			57.5	6.1	57.9	83.9
			11.3	-39.0	40.6	163.9
			35.3	-60.6	70.1	149.7
2011b	2011-06-05	D0-G1-H0-I1	62.1	-37.4	72.5	121.1
			25.0	65.1	69.7	21.0
			8.0	-39.7	40.5	168.6
			29.1	-62.8	69.2	155.2
			54.1	2.3	54.1	87.6
			33.0	25.4	41.7	52.4
2011c	2011-06-05	D0-G1-H0-I1	7.1	-39.8	40.4	169.8
			25.6	64.6	69.5	21.6
			27.4	-63.3	69.0	156.6
			60.2	-38.5	71.4	122.6
			32.8	24.8	41.1	52.9
			53.0	1.3	53.0	88.6
2011d	2011-06-05	D0-G1-H0-I1	not used (low quality)			

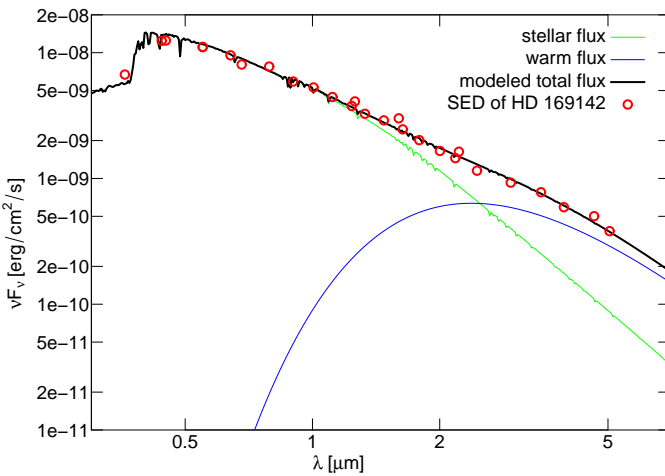


**Fig. 3.** SED of HD 169142, and our Kurucz plus blackbody fitting.

the interferometric observations, bearing in mind the fact that HD 169142 is variable in NIR. In the optical band we adopted

all the available data after confirming that there are no significant variability in the data set, which spans  $\sim 25$  years. We assumed a 5% uncertainty for each flux point.

### 3. Geometric modeling

In order to characterize the size of the NIR-emitting warm dust, as a first step we performed a modeling of the emission with a simple ring geometry. For this purpose, we first decomposed the SED to constrain the fractional contribution of the flux originating from the warm dust. This decomposition also provides a rough estimation of the dust temperature. In this section we first describe our model, and then describe the process of SED de-composition and ring-fitting. In this simple modeling, we use only band-averaged visibilities.

In our model, the optical to NIR continuum of HD 169142 arises from three origins, the central star, a sub-au dust component, and an extended halo. Following Wagner et al. (2015), we modeled the central star as a Kurucz spectrum (Kurucz 1992) with  $T = 7500$  K,  $\log g = 4$ , and  $A_v = 0$ . The sub-AU warm dust radiates thermal emission in the NIR, which we modeled as single-temperature blackbody. Cold material at much larger distance, which we generally refer to as the “halo”, scatters the

**Table 2.** Results of our modeling of the SED of HD 169142 with a Kurucz plus blackbody model. The first three parameters are free parameters in the model fitting; the others are derived quantities. The uncertainties are estimated with a bootstrapping method.

Parameter	Best-fit value
$F_h$ [ $10^{-9}$ erg sec $^{-1}$ cm $^{-2}$ ]	$14.6 \pm 0.24$
$F_w$ [ $10^{-9}$ erg sec $^{-1}$ cm $^{-2}$ ]	$0.86 \pm 0.044$
$T_d$ [K]	$1543 \pm 60$
$\chi^2_{\text{red}}$	3.16
$f_w$ [%]	$22.3 \pm 2.1$

light from the star and the warm dust, but does not emit in the NIR by itself. Therefore, the total flux of the whole system is

$$F(\lambda) = F_{\text{star}} + F_{\text{dust}} + F_{\text{halo}} = F_{\text{star}} + F_{\text{dust}} + k(F_{\text{star}} + F_{\text{dust}}), \quad (1)$$

where  $k$  is the fraction of light scattered by the halo. For simplicity, we assume the halo to have wavelength-independent albedo and that it scatters the same fraction of the stellar light and dust continuum.

### 3.1. SED decomposition

The influence of the halo component to the SED is enhancing the flux by a factor of  $1 + k$ , while not altering the shape. Therefore, it is still possible to decompose the SED into a hot photospheric component and a warm component. The free parameters in the models are the bolometric flux  $F_h$  of the hot Kurucz part, bolometric flux  $F_w$  of the warm part, and the temperature of the dust  $T_d$ . We note that  $F_h$  includes not only the flux directly from the central star, but also the scattered stellar light from the halo. Similarly,  $F_w$  includes both the contribution directly from the dust and the photons that are radiated by dust and then scattered by the halo.

We ran least-squares fitting to constrain the parameters. The best-fit model and the observations are shown in Fig. 3. The model parameters are listed in Table 2. In this model, the fraction of flux contributed by the warm component at H band was  $f_w = 22.3 \pm 2.1\%$ . This constraint was then used in the modeling of the interferometric data.

### 3.2. Ring model

In the following we utilize our interferometric measurements to extract information on the geometry of the inner disk. We used a face-on model, according to the constraints on inclination from previous observations. High-resolution direct imaging of HD 169142 (summarized in Sect. 1) has shown that the outer disk is nearly face-on. Modeling of  $^{12}\text{CO}$  line emission (Raman et al. 2006) gave an estimation of  $i \approx 13^\circ$  for the outer disk. Inclination of the inner disk has been estimated to be  $i \approx 22^\circ$  with PIONIER observations (Lazareff et al. 2017). All these observations indicate that the inner and outer disks are nearly aligned to each other and both are nearly face-on. Our model consists of the star, an infinitesimally narrow circular ring, and an over-resolved halo component. The total visibility is therefore

$$V = f_{\text{star}} V_{\text{star}} + f_{\text{ring}} V_{\text{ring}} + f_{\text{halo}} V_{\text{halo}}, \quad (2)$$

where  $f_{\text{star}}$ ,  $f_{\text{ring}}$ , and  $f_{\text{halo}}$  are the fractions of flux contributed by each component. The fractions follow the rule  $f_{\text{star}} + f_{\text{ring}} + f_{\text{halo}} \equiv 1$ . We assumed that the star is completely unresolved and the halo is completely overresolved, so that  $V_{\text{star}} \equiv 1$ , and  $V_{\text{halo}} \equiv 0$ . Measuring at wavelength  $\lambda$ , with a baseline of length  $B$ , the visibility of the circular ring is the Bessel function

$$V_{\text{ring}} = J_0(2\pi\nu r_{\text{ring}}), \quad (3)$$

where  $r_{\text{ring}}$  is the angular ring radius, and  $\nu = B/\lambda$  is the spatial frequency.  $f_{\text{halo}}$  and  $r_{\text{ring}}$  are free model parameters. The other two flux fractions are derived as

$$f_{\text{ring}} = f_w(1 - f_{\text{halo}}) \quad (4)$$

and

$$f_{\text{star}} = (1 - f_w)(1 - f_{\text{halo}}), \quad (5)$$

where  $f_w$  is constrained by the SED decomposition (see Sect. 3.1). Our best-fit model and error estimations are presented in Table 3 and Fig. 2. The uncertainties are estimated with a bootstrapping method. In each of our bootstrapping samples, both the fluxes and the visibilities are re-sampled. Therefore, the error estimations account not only for the uncertainties in visibility measurement, but also for the uncertainties in the photometry.

In the best-fit model, the ring radius is  $\sim 0.08$  au, which is in rough agreement with the dust sublimation radius assuming  $T_{\text{sub}} \sim 1500$  K. The fraction between bolometric flux of the warm and the photospheric component is  $F_w/F_h \sim 0.06$ . Therefore, the model is consistent with warm dust absorbing  $\sim 6\%$  of all the stellar light and re-emitting the energy in the NIR.

A halo component is clearly needed to account for the fact that the visibility is already lower than 1.0 at the shortest baselines ( $B \sim 10$  m). In the best-fit model the flux fraction of the halo is  $\sim 12\%$ , only slightly higher than the estimate of  $\sim 8\%$  in Lazareff et al. (2017). Halo components, representing scattered light from extended ( $> 1$  au) cold material, are frequently detected in NIR interferometric observations of Herbig stars, with typical flux ratios of 5%–20% (e.g., Monnier et al. 2006; Chen et al. 2012; Kreplin et al. 2016). Plausible origins of the halo material include an infalling remnant envelope, dust entrained in the stellar wind or outflow (Monnier et al. 2006), or a flaring outer disk that scatters the stellar light (Pinte et al. 2008). In the particular case of HD 169142, stellar light scattered from the outer disk has been detected in direct imaging, and such imaging has indeed been employed to reveal the complex disk structure (Quanz et al. 2013). The outer disk's scale height of  $\sim 0.1$  (Monnier et al. 2017) at  $R \sim 30$  au also indicates its capability of scattering  $\sim 10\%$  of stellar light. Therefore, it is likely that the outer disk is the main contributor to the halo light in HD 169142.

To summarize, our geometric modeling indicates that the NIR brightness distribution in HD 169142 can be well interpreted with a central star, passively heated warm dust circular-symmetrically distributed around the star, and an extended scattering component. Therefore, in the next step we set up our radiative transfer models within this frame, and perform numerical simulation in order to further constrain the properties of the warm dust.

## 4. Monte-Carlo radiative transfer modeling of the interferometric data and the SED

In this section we present a more physical modeling approach. In our radiative transfer modeling, we have tried to reproduce the

**Table 3.** Results of our modeling of the visibilities of HD 169142 with star-ring-halo model. The first two parameters are free parameters in the model fitting; the others are derived quantities. The uncertainties are estimated with a bootstrapping method.

Parameter	Best-fit value
$r_{\text{ring}}$ [mas]	$0.655 \pm 0.061$
$f_{\text{halo}}$ [%]	$11.9 \pm 0.6$
$\chi^2_{\text{red}}$	0.91
$f_{\text{star}}$ [%]	$68.5 \pm 1.9$
$f_{\text{ring}}$ [%]	$19.6 \pm 1.9$
$L_{\text{star}}$ [ $L_{\odot}$ ( $\frac{d}{117 \text{ pc}}$ ) $^2$ ]	$5.49 \pm 0.10$
$R_{\text{ring}}$ [au ( $\frac{d}{117 \text{ pc}}$ )]	$0.077 \pm 0.007$

interferometric data and the SED simultaneously in the optical-NIR with a disk model consisting of a sub-au inner disk and a scattering halo component.

For the dust disk, we assumed a power-law radial distribution for its surface density  $\Sigma$ ,

$$\Sigma(r) = \Sigma_{\text{in}} \left( \frac{r}{R_{\text{in}}} \right)^p, \quad R_{\text{in}} < r < R_{\text{out}}, \quad (6)$$

where  $\Sigma_{\text{in}}$  is the surface density at the inner radius  $R_{\text{in}}$ ,  $p$  is the power-law exponent, and  $R_{\text{out}}$  is the outer radius of the dust disk. We assumed the vertical dust density distribution to be a Gaussian function, and the resulting density structure of the disk is

$$\rho(r, z) = \Sigma(r) \frac{1}{\sqrt{2\pi}H} \exp\left(-\frac{z^2}{2H^2}\right), \quad (7)$$

where  $\rho(r, z)$  denotes the dust density as a function of  $r$  and the height  $z$  above the mid-plane, and  $H$  is the scale height. We assumed that the dependence of  $H$  on  $r$  is also a power-law,

$$h(r) \equiv \frac{H(r)}{r} = h_{\text{in}} \left( \frac{r}{R_{\text{in}}} \right)^q, \quad (8)$$

where  $h(r)$  is the dimensionless scale height,  $h_{\text{in}}$  is the dimensionless scale height at the inner radius, and  $q$  is the power-law index.

The main purpose of this paper is to constrain the properties of the inner disk, including its size, geometry, and dust composition with our new NIR interferometric data. Therefore, we tested two types of models for the inner sub-au region: optically thin dust with a large scale height (model type A), or optically thick dust with a flat geometry (model type B). We used a mixture of amorphous carbon (Jager et al. 1998) and astronomical silicate (Draine & Lee 1984), and tested different dust compositions by adjusting the parameter  $f_{\text{carbon}}$  (fraction of carbon). We assumed a power-law grain size distribution

$$n(a) \propto a^n, \quad a_{\text{min}} < a < a_{\text{max}}. \quad (9)$$

With the limited information available, it is impossible to constrain the parameters  $a_{\text{min}}$ ,  $a_{\text{max}}$ , and  $n$  simultaneously. We chose to use fixed size limits  $a_{\text{min}} = 0.01 \mu\text{m}$  and  $a_{\text{max}} = 10^3 \mu\text{m}$ , and used the power-law index  $n$  to control the fraction of sub-mm and larger grains.

We tested different stellar luminosities around the value estimated in Sect. 3.2. A simplification in the geometric modeling

is that the scattering of stellar light from the inner dust is neglected. When this process is fully considered in our radiative transfer modeling, the best-fit luminosity value is found to be slightly lower.

For each set of stellar and inner disk parameters, we performed Monte-Carlo radiative transfer (MCRT) simulation with RADMC3D, rendering the spatial and spectral distribution of the radiation. The scattered light from larger-scale material (corresponding to the “halo” component in the geometric model) is not directly included in the MCRT simulation, but taken into consideration in a parametrized way. We assumed the halo to scatter the light from the central star and the inner disk with a wavelength-independent fraction  $k$ . Therefore, the effects of the halo are that it increases the total flux from the system by a factor of  $1 + k$ , and reduces the visibilities by the same factor. Therefore, after each MCRT run, the final SED and  $V^2$  can be analytically calculated. We used a fixed  $k = 13\%$ , which is derived from  $f_{\text{halo}} = \frac{k}{1+k} = 12\%$  in Sect. 3.2.

#### 4.1. Fitting with model type A (optically thin inner disk)

In the optically thin case, the amount of stellar light that the dust absorbs and re-emits in the NIR is roughly proportional to the optical depth  $\tau$ , and to the scale height  $h_{\text{in}}$  of the dust. Obviously there is a degeneracy between the two parameters. We chose to use a fixed  $h_{\text{in}} = 0.6$ , and use  $\tau$  as a proxy to the amount of NIR excess.

While our interferometric data set constrained the size of the inner NIR-emitting region, it did not contain enough information to constrain the radial dust distribution in detail, because the inner dust is only partially resolved even with the longest baselines. This ambiguity is reflected in a degeneracy between the relative width  $W_{\text{ring}} = (R_{\text{out}} - R_{\text{in}})/R_{\text{in}}$  and the inner radius  $R_{\text{in}}$ , as demonstrated in Appendix A.2. We therefore chose to use a fixed relative width  $W_{\text{ring}} = 0.5$  and use  $R_{\text{in}}$  to characterize the disk size.

We tested  $\sim 7000$  models in order to find a model of type A that can approximately reproduce the NIR visibilities and the NIR SED. The best-fit model AF1 is shown in Fig. 4. We present in Appendix A.1 a description of the parameter scanning process, in which we start the scanning from broad parameter ranges and then narrow down to a finer parameter grid.

We find that both the inner disk radius and the dust grain size distribution are well constrained by the modeling. In the best-fit model, the inner disk has an  $R_{\text{in}}$  of 0.07 au, and a power-law index  $n$  of  $-2$  for the grain size distribution. Fitting of similar quality can be achieved for any distribution with  $n \geq -3$ . Models with  $n \leq -3.5$  have much higher  $\chi^2$  and are excluded. The power law with  $n \geq -3$  means that the dust consists mainly of large grains with  $a > 1 \mu\text{m}$ .

In the following we discuss the reason why the modeling is sensitive to the parameter  $n$ . The radiative-equilibrium temperature of optically thin dust irradiated by a star with luminosity  $L_*$  at a distance of  $R$  is (see, e.g., Dullemond & Monnier 2010)

$$T = \left( \frac{L_*}{16\pi\sigma\epsilon R^2} \right)^{1/4}, \quad (10)$$

where the cooling parameter  $\epsilon$  is the ratio between the absorption coefficient of the dust in the NIR and that in the optical.  $\sigma$  is the Stefan-Boltzmann constant. Therefore, for a given  $R$  (constrained with the interferometric observations), the color of the NIR dust emission is sensitive to  $\epsilon$ , which in turn depends on the grain size distribution. For example, dust with  $a_{\text{min}} = 0.01 \mu\text{m}$ ,

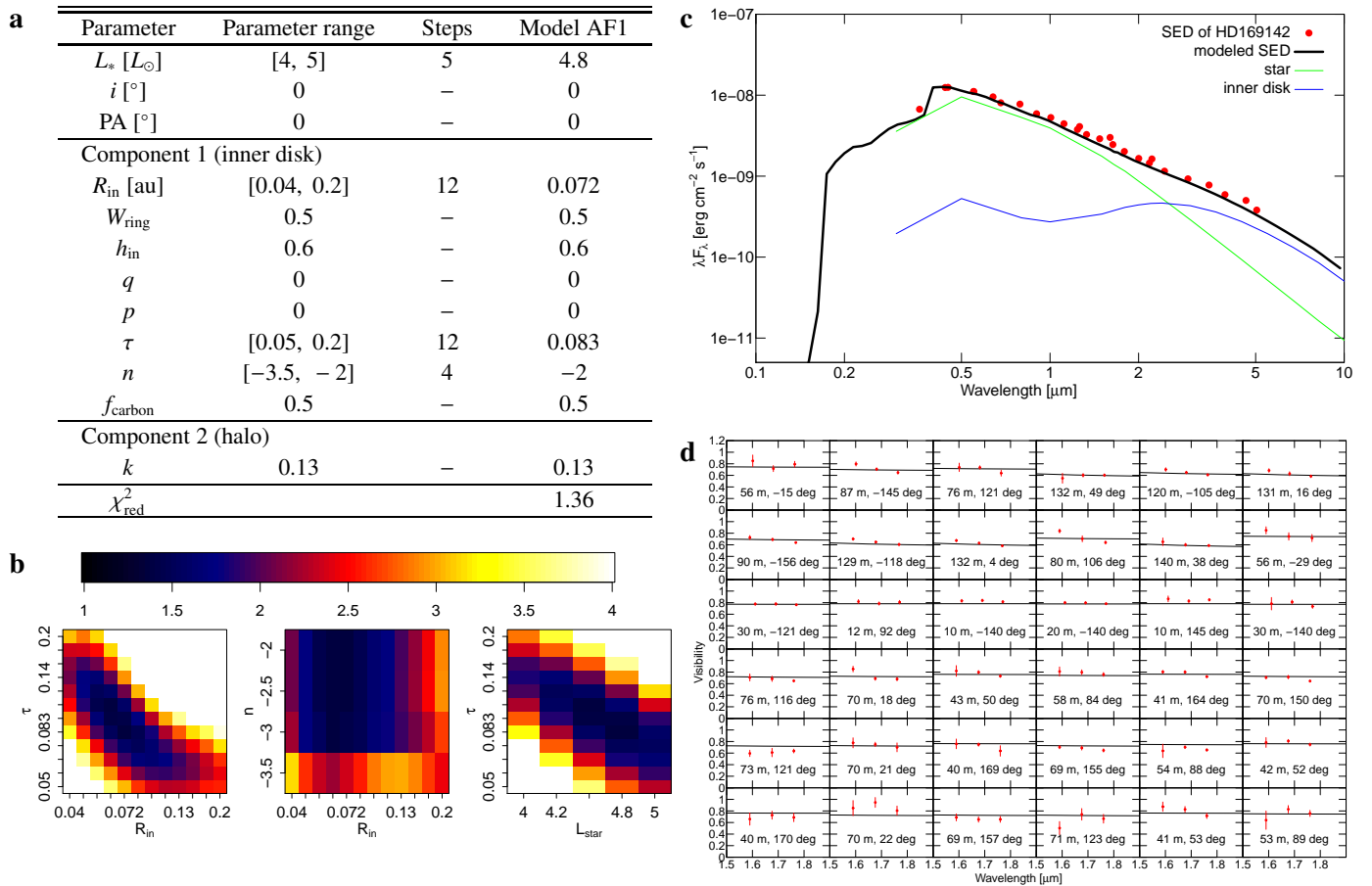


**Fig. 4.** Model scanning run AF (optically thin inner disk), and the model parameters of the best model AF1 with minimum  $\chi^2_{\text{red}}$ , which is calculated by comparing each model with the data set.

*a*: Parameter ranges of model scanning run AF, number of tested parameter values (steps) per parameter, and parameters of the best model AF1. The listed parameters are:

$L_*$  = stellar luminosity ,

$i$  = inclination of the disk,

PA = positional angle of rotation axis the disk,

and the following parameters for the inner sub-AU disk,

$R_{\text{in}}$  = inner radius of the inner disk ,

$W_{\text{ring}} = (R_{\text{out}} - R_{\text{in}})/R_{\text{in}}$  (relative radial width of the inner component),

$R_{\text{out}}$  = outer radius of the inner disk ,

$h_{\text{in}}$  = scale height of the inner disk at its inner radius,

$q$  = scale-height power-law index of the inner disk,

$p$  = surface-density power-law index,

$\tau$  = Planck-averaged midplane optical depth at 7500 K,

$n$  = power-law index of grain size distribution,

$f_{\text{carbon}}$  = fraction of carbon in the dust.

*b*:  $\chi^2_{\text{red}}$  maps of Model run AF. For each subset of parameters, the  $\chi^2_{\text{red}}$  shown is the lowest value for all combinations with other parameters. For example, for each pair of ( $R_{\text{in}}$ ,  $\tau$ ) values, the  $\chi^2_{\text{red}}$  values for all possible ( $L_*$ ,  $n$ ,  $f_{\text{carbon}}$ ) combinations within the described ranges were compared and the minimum value found is plotted into the map at left panel.

*c*: SED of HD 169142. The lines denote the model contributions from different radial regions. The red dots are the observations. 5% uncertainty is assumed for each observation.

*d*: NIR visibilities (red dots: observations; black lines: model) from our VLTI/PIONIER observations.

$a_{\text{max}} = 10^3 \mu\text{m}$ , and  $n = -5$  has  $\epsilon \approx 0.2$ , which causes an increase of temperature by a factor of  $\epsilon^{-1/4} \approx 1.5$  compared to gray dust. Such increase will have a strong effect on the model SED.

For grain sizes larger than  $1 \mu\text{m}$ , the dust will have a flat opacity curve in the optical-NIR range, and therefore

$\epsilon \sim 1$ , independent of chemical composition (see, e.g., Fig. 8 in Dullemond & Monnier 2010). Therefore, our modeling sets no constraint on  $f_{\text{carbon}}$ . We cannot get complementary constraints on the chemical composition from spectroscopic study around the  $10 \mu\text{m}$  silicate feature, because the N-band

emission in HD 169142 is dominated by strong PAH features (Maaskant et al. 2014).

In this optically thin case, the dust temperature decreases smoothly with the distance from the central star,  $T \propto r^{-1/2}$ . For the narrow radial width  $W_{\text{ring}} = 0.5$  that we assumed, the range of temperatures is also narrow. In the best-fit model, the dust temperature ranges between  $\sim 1300$  K at the outer edge and  $\sim 1600$  K at the inner edge.

#### 4.2. Fitting with model type B (optically thick inner disk)

In the optically thick case, the amount of stellar light that the dust absorbs and re-emits in the NIR becomes insensitive to the optical depth  $\tau$  of the dust, and depends mainly on the scale height  $h_{\text{in}}$  of the dust. We therefore use a fixed  $\tau = 10^3$ , and use  $h_{\text{in}}$  to adjust the amount of NIR excess.

We tested  $\sim 2000$  models in order to find a model of type B that can approximately reproduce the NIR visibilities and the NIR SED. The best-fit model BF1 is shown in Fig. 5. The parameter scanning process is described in Appendix A.2.

While the size of the inner rim is tightly constrained to be  $\sim 0.06$  au, the dust grain size distribution is not constrained at all. The temperature distribution of passively heated optically thick dust is highly inhomogeneous, with hot surface layers covering the cold interior region. The color of the overall emission is determined by complicated radiative transfer processes involving both the surface layers and the interior. Numerical studies of the radiative transfer processes show that the overall color is insensitive to  $\epsilon$  (see e.g., Dullemond & Monnier 2010; Chen et al. 2016).

The hottest part in the best-fit model is the surface layer of the inner rim. This layer is directly irradiated by the central star and has a temperature of  $\sim 2400$  K. We found that this surface temperature is also insensitive to  $n$  or  $\epsilon$ , in the  $\epsilon$  range we tested ( $0.2 \leq \epsilon \leq 1$ ). The surface temperature is higher than the sublimation temperature of silicate or carbonaceous material. Therefore, to establish a self-consistent model, refractory dust species that can exist at  $\sim 2400$  K should be added to the model BF1. We did not perform radiative transfer computing for a model including refractory dust, because our modeling already shows that neither the surface temperature nor the modeled observables are sensitive to the choice of species. Therefore, our conclusion is that the observations can be reproduced by an optically thick dust, with inner rim radius  $\sim 0.06$  au and scale height  $H/R \sim 0.03$ , consisting of a mixture of refractory dust and normal dust (silicate and carbonaceous material).

## 5. Discussion

### 5.1. Constraints on dust properties

The inner sub-AU disk of HD 169142 is likely in rapid variation (Wagner et al. 2015). The interferometric PIONIER observations allow us to study its structure and dust properties around the years 2011-2013. Our geometric modeling shows that its NIR excess arises from warm dust ( $\sim 1500$  K) at a distance of  $\sim 0.08$  au from the central star, consistent with dust sublimation radius for optically thin gray dust. With radiative transfer modeling we found that the observations are consistent with optically thin gray dust lying at  $R_{\text{in}} \sim 0.07$  au. In the best-fit model of this type (model AF1), the temperature of the dust is between  $\sim 1300$  K and  $\sim 1600$  K. Therefore, both the location and temperature of dust in model AF1 is similar to that estimated in geometric modeling. Models with sub-micron optically thin dust

are excluded because such dust will have much higher temperature at similar distance.

A model with optically thick dust with inner rim at  $R_{\text{in}} \sim 0.06$  au can also reproduce the observations. However, due to the highly inhomogeneous temperature distribution, with  $T \sim 2400$  K in its hottest part, this model is plausible only if refractory dust species exist in the inner disk. Evidence for the existence of refractory dust has been found in other Herbig stars. For example, interferometric study of HD 163296 (Benisty et al. 2010a) indicates inner refractory dust with a temperature of 2100–2300 K.

Because models with either optically thin or thick disks can reproduce the data, it is obvious that a hybrid model consisting of both optically thin and thick components is also possible, and the fraction of NIR light contributed by each part is unconstrained. In such a model, gray dust is again preferred to sub-micron dust.

The inner disk size in each of our models is significantly smaller than the size of  $R_{\text{in}} \sim 0.19$  au<sup>3</sup> in the previous model in Wagner et al. (2015). The fact that their model also reproduced the NIR SED reflects a degeneracy between the radius  $R_{\text{in}}$  and the cooling parameter  $\epsilon$  in SED modeling. While increasing  $R_{\text{in}}$  will decrease the dust temperature and make the dust emission redder, using dust with lower  $\epsilon$  will increase the temperature of optically thin dust and make the emission bluer, balancing the effect of increasing  $R_{\text{in}}$ . In the present work, the interferometric observations constrain  $R_{\text{in}}$  and therefore break the degeneracy.

### 5.2. NIR variability of the inner disk

In the scenario proposed by Wagner et al. (2015), the NIR variability in HD 169142 is caused by changes in the dust distribution of an optically thin component, while the optically thick core in their models remains constant. They proposed three models for the pre-2000 state of HD 169142, in which the optically thin components differ from the post-2000 state in scale height, radial width, and/or dust density. Despite the differences between these models, a common character in them is that the optically thin dust always has higher mass than in the post-2000 state by a factor of at least two, indicating that this component is dissipating on a short timescale of  $\sim 10$  yr. Their argument against the variation caused by varying height of an optically thick dust is that such a structural change, while changing the ability of the dust in reprocessing stellar light into NIR emission, will also cause varying shadowing on the outer disk and lead to variations in the emission from the outer disk. The lack of MIR-FIR variation in HD 169142 (Kóspál et al. 2012; Wagner et al. 2015) therefore may disfavor a varying optically thick dust.

If the NIR variation in HD 169142 is solely due to variation in the optically thin component, then our two RT models for the inner dust in low state will correspond to two scenarios (Fig. 6) for the readjusting of the inner dust. In scenario 1, the inner dust is optically thin in the pre-2000 state and has lost part of its mass in the post-2000 state (model AF1). In scenario 2, the inner dust consists of an optically thin component and an optically thick core in the pre-2000 state. The optically thin component has completely dissipated after 2000 (model BF1), while the optically thick core remains constant. In both scenarios, the NIR variabilities arise solely from changes affecting the optically thin component.

The inner disk will probably continue varying in the following decades. Following scenario 1, if the inner optically thin dust continues to lose its mass with the current mass-loss rate, then

<sup>3</sup> scaled to  $D = 117$  pc.

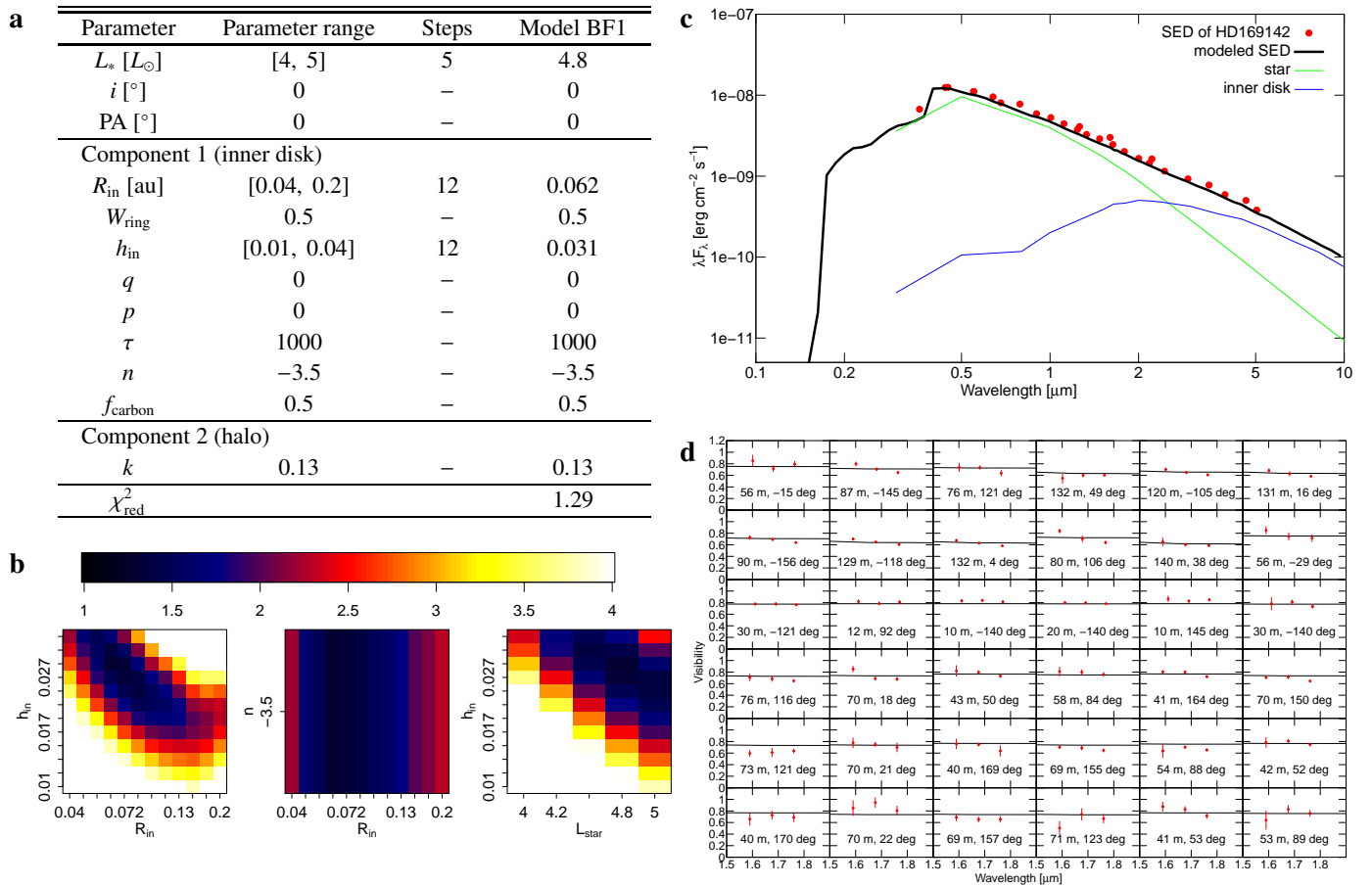


**Fig. 5.** As Fig. 4, but for model run BF, compared with the data set. Model BF1 is the model with minimum  $\chi^2_{\text{red}}$ .

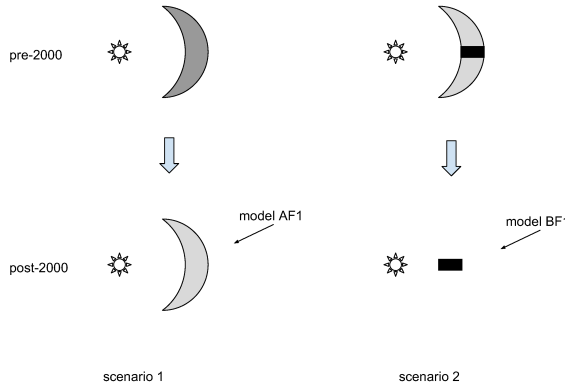


**Fig. 6.** Sketch of the scenarios for the evolution of the inner sub-AU region in HD 169142.

the disk will evolve into a transitional disk within only several decades, and this would be an extremely interesting case of disk evolution. However, such a timescale is much shorter than the expected evolutional timescale of  $\sim 10^5$  yr for disks in the pre-transitional and transitional phases. It is also surprising from statistical point of view that an object is caught in this very short evolution phase which lasts for less than 100 years, considering the small number of Herbig stars observed. Therefore, it is

more likely that the fading observed in the past decades is only one episode in a series of fluctuations in dust amount and in its emission. This can happen if the dust is being replenished in a time-dependent process. Collisions between larger bodies can provide secondary dust to the inner region of pre-transitional objects (Grady et al. 2009; Eisner et al. 2006; Krijt & Dominik 2011). Such replenishing can be occasionally enhanced by a collision between the largest parental bodies or by gravitational stirring from a nearby planet (Krivov 2010). Small amounts of dust from the outer disk passing through the planet-induced gap region (Pinilla et al. 2016) can also be an unsteady supply of inner NIR-emitting dust and cause NIR variations on timescale of several decades (e.g., in the case of GW Ori, Fang et al. 2014).

For scenario 2, the optically thin dust may be replenished by disk wind or by material lifted up from the optically thick disk by turbulent dynamic processes, and these unsteady processes can cause variability on timescale of months or years (Bary et al. 2009). Another possible cause of future NIR variability is changing of height of the optically thick component, though this does not seem to have happened in the past decades, as argued by Wagner et al. (2015).

Further NIR photometric observations, which constrain the amount and temperature of the hot dust, and NIR interferometry, which constrains the radial location and grain size distribution of the dust, will provide useful information on the nature of variabilities in the inner region. Photometry at MIR-FIR wavelengths will be useful in revealing the varying shadowing on the outer disk, in case there will be any change in the height of the inner optically thick component.

### 5.3. Correlation between dust grain size and gap size?

Statistical studies on how the dust grain size distribution depends on other disk parameters can provide useful constraint on the theoretical modeling of disk evolution. In the following we compare our results with inner dust properties in several other Herbig stars with pre-transitional disks.

HD 100546 has a gap region with a width of  $\sim 10$  au (Benisty et al. 2010b; Tatulli et al. 2011; Mulders et al. 2013). The inner dust likely consists of dust grains with size around one micron ( $[0.1, 5]$   $\mu\text{m}$  and  $n = -3.5$  in Benisty et al. 2010b and Tatulli et al. 2011,  $[0.1, 1.5]$   $\mu\text{m}$  in Mulders et al. 2013). A narrower gap region has been found in HD 139614 (Matter et al. 2014, 2016) from  $\sim 2.5$  au to  $\sim 5.7$  au. The dust composition of the inner dust in their radiative transfer model is 20% graphite with small grain size ( $[0.05, 0.2]$   $\mu\text{m}$ ) and 80% silicate with large grain size ( $[5, 20]$   $\mu\text{m}$ ). Due to the much larger opacity of the small grains, the optical-NIR opacity is dominated by the small graphite grain and the silicate is introduced purely for interpreting the N-band silicate feature. For HD 144432 (Chen et al. 2016), a even narrower gap between  $\sim 0.3$  au and  $\sim 1.4$  au was found, and the NIR emitting material is likely optically thin dust consisting of mainly sub-micron grains.

Comparing our model A with the results for the three objects listed above, there might be a trend that objects with wider gaps tend to have larger grain size in their inner disks. However, a decisive conclusion cannot be made with this small sample. Moreover, we cannot strictly exclude the possibility that the inner dust in HD 169142 is optically thick, with small grain size, and containing refractory species. To confirm whether there is a trend for grain size to grow simultaneously with disk gap size, more objects are needed to be similarly studied.

## 6. Summary and conclusions

In this paper we present a study of the dust properties in the innermost sub- $\text{au}$  region in the disk of the Herbig star HD 169142, using interferometric observations of the object with VLTI/PIONIER. The object has been found to be variable in the NIR, and has evolved from a pre-2000 state with higher NIR excess to a post-2000 state with lower NIR excess. The VLTI/PIONIER observations were performed in the 2011 and 2013, when the object was already in low state. We performed geometric modeling and Monte-Carlo radiative transfer modeling of the data, complemented with SED data from literature. The following results were obtained.

Both our geometric modeling and the Monte-Carlo radiative transfer modeling indicate that the NIR-emitting hot dust is located at  $\sim 0.07$  au from the central star. Our Monte-Carlo radiative transfer modeling shows that the SED and visibilities can be simultaneously reproduced with an optically thin dust model with large grain size ( $\geq 1.0$   $\mu\text{m}$ ), or with an optically thick component at similar location. Optically thin dust containing smaller grains is excluded by our modeling, because such a dust at the location of  $\sim 0.07$  au would be overheated to a higher temperature (compared to gray dust), therefore causing the modeled SED to be bluer than the observed one. If the dust is optically thick, then it must contain refractive species, so that the hot surface layer is not destroyed. Grain size distribution is not constrained in the optically thick case.

Based on the modeling, we discussed the possible scenarios for the object to evolve from its pre-2000 state (with higher NIR excess) to its current state. In our scenario 1, the inner dust is optically thin in the pre-2000 state and lost part of its mass

later. In scenario 2, the inner dust consists of an optically thin component and an optically thick core in the pre-2000 state, and then lost the optically thin component later. In both scenarios, the NIR variability arises solely from changes affecting the optically thin component. We argue that further IR photometric and interferometric observations will help to reduce the ambiguities in the current study.

Statistical studies of dependence of dust grain size distribution on other disk parameters can provide helpful information for understanding disk evolution. By comparing our results with other interferometric studies that constrained the dust grain size in the inner region of pre-transitional disks, there seems to be a positive correlation between gap width and grain size of inner dust. However, more observations on larger samples are needed for a firm conclusion.

*Acknowledgements.* This work was supported by the Momentum grant of the MTA CSFK Lendület Disk Research Group. The authors are thankful to the generous help and useful comments from Myriam Benisty. The comments from an anonymous referee helped to improve the quality of the paper.

## References

Bary, J. S., Leisenring, J. M., & Skrutskie, M. F. 2009, *ApJ*, 706, L168  
 Benisty, M., Natta, A., Isella, A., et al. 2010a, *A&A*, 511, A74  
 Benisty, M., Tatulli, E., Ménard, F., & Swain, M. R. 2010b, *A&A*, 511, A75  
 Biller, B. A., Males, J., Rodigas, T., et al. 2014, *ApJ*, 792, L22  
 Chen, L., Kreplin, A., Wang, Y., et al. 2012, *A&A*, 541, A104  
 Chen, L., Kreplin, A., Weigelt, G., et al. 2016, *A&A*, 586, A54  
 Draine, B. T. & Lee, H. M. 1984, *ApJ*, 285, 89  
 Dullemond, C. P. & Monnier, J. D. 2010, *ARA&A*, 48, 205  
 Eisner, J. A., Chiang, E. I., & Hillenbrand, L. A. 2006, *ApJ*, 637, L133  
 Fang, M., Sicilia-Aguilar, A., Roccatagliata, V., et al. 2014, *A&A*, 570, A118  
 Fedele, D., Carney, M., Hogerheijde, M. R., et al. 2017, *A&A*, 600, A72  
 Gaia Collaboration, Brown, A. G. A., Vallenari, A., et al. 2016, *A&A*, 595, A2  
 Grady, C. A., Schneider, G., Sitko, M. L., et al. 2009, *ApJ*, 699, 1822  
 Haubois, X., Bernaud, P., Mella, G., et al. 2014, in *Proc. SPIE*, Vol. 9146, Optical and Infrared Interferometry IV, 914600  
 Honda, M., Maaskant, K., Okamoto, Y. K., et al. 2012, *ApJ*, 752, 143  
 Isella, A., Guidi, G., Testi, L., et al. 2016, *Physical Review Letters*, 117, 251101  
 Jager, C., Mutschke, H., & Henning, T. 1998, *A&A*, 332, 291  
 Kóspál, Á., Ábrahám, P., Acosta-Pulido, J. A., et al. 2012, *ApJS*, 201, 11  
 Kreplin, A., Madlener, D., Chen, L., et al. 2016, *A&A*, 590, A96  
 Krijt, S. & Dominik, C. 2011, *A&A*, 531, A80  
 Krivov, A. V. 2010, *Research in Astronomy and Astrophysics*, 10, 383  
 Kurucz, R. L. 1992, in *IAU Symposium*, Vol. 149, The Stellar Populations of Galaxies, ed. B. Barbuy & A. Renzini, 225  
 Lazareff, B., Berger, J.-P., Kluska, J., et al. 2017, *A&A*, 599, A85  
 Le Bouquin, J.-B., Berger, J.-P., Lazareff, B., et al. 2011, *A&A*, 535, A67  
 Maaskant, K. M., Honda, M., Waters, L. B. F. M., et al. 2013, *A&A*, 555, A64  
 Maaskant, K. M., Min, M., Waters, L. B. F. M., & Tielens, A. G. G. M. 2014, *A&A*, 563, A78  
 Macías, E., Anglada, G., Osorio, M., et al. 2017, *ApJ*, 838, 97  
 Matter, A., Labadie, L., Augereau, J. C., et al. 2016, *A&A*, 586, A11  
 Matter, A., Labadie, L., Kreplin, A., et al. 2014, *A&A*, 561, A26  
 Meeus, G., Waters, L. B. F. M., Bouwman, J., et al. 2001, *A&A*, 365, 476  
 Menu, J., van Boekel, R., Henning, T., et al. 2015, *A&A*, 581, A107  
 Momose, M., Morita, A., Fukagawa, M., et al. 2015, *PASJ*, 67, 83  
 Monnier, J. D., Berger, J.-P., Millan-Gabet, R., et al. 2006, *ApJ*, 647, 444  
 Monnier, J. D., Harries, T. J., Aarnio, A., et al. 2017, *ApJ*, 838, 20  
 Mulders, G. D., Paardekooper, S.-J., Panić, O., et al. 2013, *A&A*, 557, A68  
 Osorio, M., Anglada, G., Carrasco-González, C., et al. 2014, *ApJ*, 791, L36  
 Pinilla, P., Klarmann, L., Birnstiel, T., et al. 2016, *A&A*, 585, A35  
 Pinte, C., Ménard, F., Berger, J. P., Benisty, M., & Malbet, F. 2008, *ApJ*, 673, L63  
 Quanz, S. P., Avenhaus, H., Buenzli, E., et al. 2013, *ApJ*, 766, L2  
 Raman, A., Lisanti, M., Wilner, D. J., Qi, C., & Hogerheijde, M. 2006, *AJ*, 131, 2290  
 Reggiani, M., Quanz, S. P., Meyer, M. R., et al. 2014, *ApJ*, 792, L23  
 Tatulli, E., Benisty, M., Ménard, F., et al. 2011, *A&A*, 531, A1  
 van der Marel, N., van Dishoeck, E. F., Bruderer, S., et al. 2013, *Science*, 340, 1199  
 Wagner, K. R., Sitko, M. L., Grady, C. A., et al. 2015, *ApJ*, 798, 94

## Appendix A: Detailed description of the fitting process with Monte-Carlo radiative transfer models

### A.1. Fitting with model type A (optically thin inner disk)

In our model scanning run A, we tested  $4 \times 8 \times 7 \times 3 \times 7 = 4704$  models with wide ranges of inner disk parameters. We focused on testing different values of  $L_*$ ,  $R_{\text{in}}$ ,  $\tau$ ,  $n$ , and  $f_{\text{carbon}}$ , and kept other parameters fixed. The parameter ranges and results are shown in Fig. A.1. The model A1 approximately reproduces the whole data set with  $\chi^2_{\text{red}} = 1.53$ .

We then tested models in narrower parameter ranges to further constrain the parameters. Because we found that the model results are insensitive to  $f_{\text{carbon}}$ , from then on we fixed it to  $f_{\text{carbon}} = 0.5$ . In our model scanning run AF, we tested  $5 \times 12 \times 12 \times 4 = 2880$  models. The parameter ranges and results are shown in Fig. 4. The model AF1 approximately reproduces the whole data set with  $\chi^2_{\text{red}} = 1.36$ .

### A.2. Parameter study on the effects of radial width in model type A

The purpose of our model scanning run AW is to test the effects of altering the radial width  $W_{\text{ring}}$  of the inner optically thin dust. In this run we fixed most of the parameters to those in model AF1, and scan different values only for  $W_{\text{ring}}$ ,  $R_{\text{in}}$ , and  $n$ , testing  $21 \times 6 \times 7 = 882$  models. The parameter ranges and results are shown in Fig. A.2. A degeneracy between  $W_{\text{ring}}$  and  $R_{\text{in}}$  is seen in the results. For any given  $W_{\text{ring}}$ , a value of  $R_{\text{in}}$  can be found so that the distance of NIR-emitting dust to the central star, on an average sense, is similar to that in model AF1. All such  $(W_{\text{ring}}, R_{\text{in}})$  pairs will lead to similar model predictions, including visibilities and overall color of the dust. This ambiguity is related to the fact that the available interferometric observations only partially resolved the inner dust of HD 169142. Despite this ambiguity, the constraint on dust grain size is robust and insensitive to the choice of  $W_{\text{ring}}$  (see Fig. A.2b).

### A.3. Fitting with model type B (optically thick inner disk)

In our model scanning run B, we tested  $4 \times 8 \times 6 \times 7 = 1344$  models with wide ranges of inner disk parameters. We focused on testing different values of  $L_*$ ,  $R_{\text{in}}$ ,  $h_{\text{in}}$ , and  $n$ , and kept other parameters fixed. The parameter ranges and results are shown in Fig. A.3. The model B1 approximately reproduces the whole data set with  $\chi^2_{\text{red}} = 1.35$ .

We then tested models in narrower parameter ranges to further constrain the parameters. Because we found that the model results are insensitive to  $n$  for this type of model, we now fix it to  $n = -3.5$ . In our model scanning run BF, we tested  $5 \times 12 \times 12 = 720$  models. The parameter ranges and results are shown in Fig. 5. The model BF1 approximately reproduces the whole data set with  $\chi^2_{\text{red}} = 1.29$ .

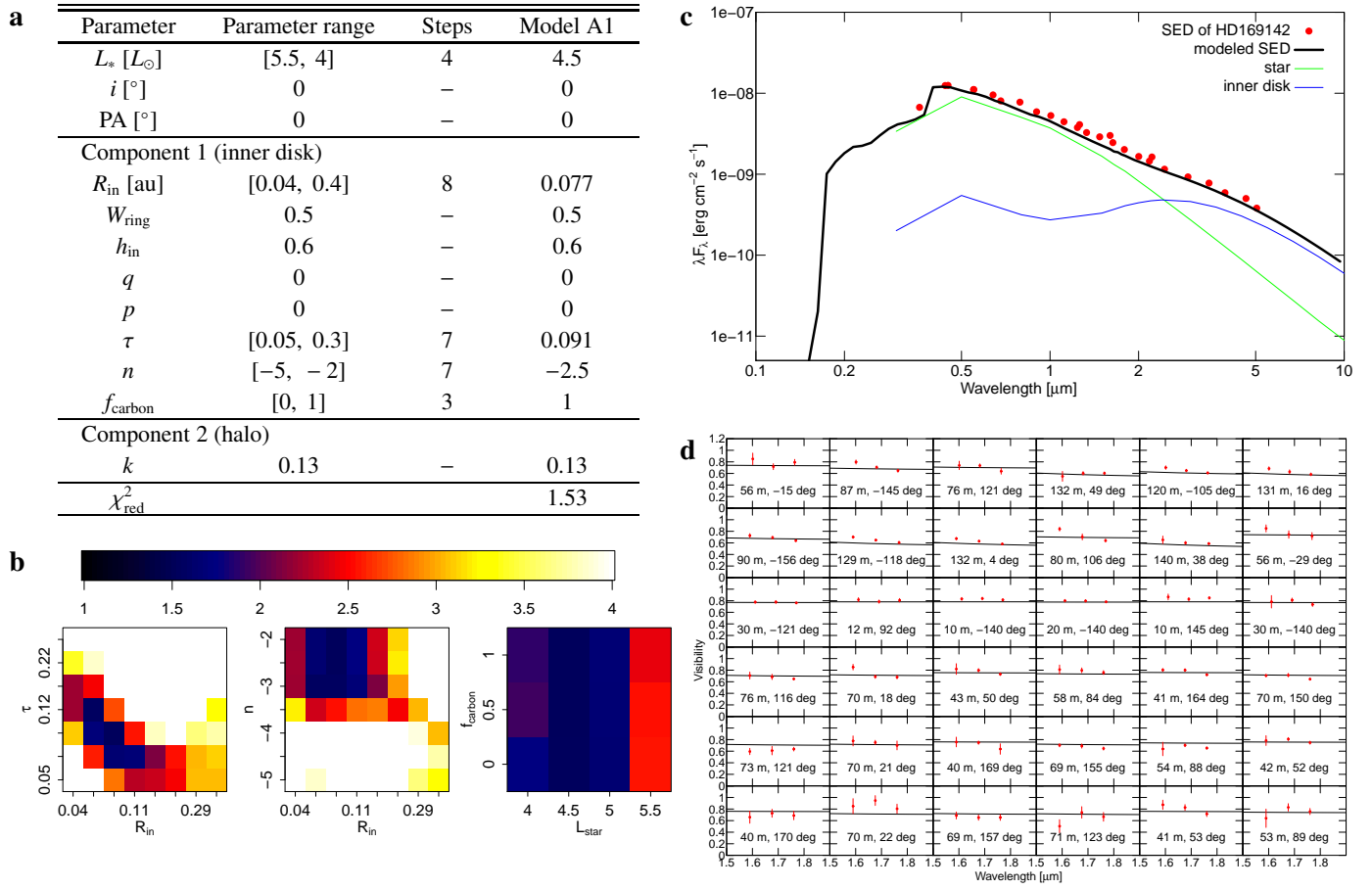


**Fig. A.1.** As Fig. 4, but for model run A, compared with the data set. Model A1 is the model with minimum  $\chi^2_{\text{red}}$ .

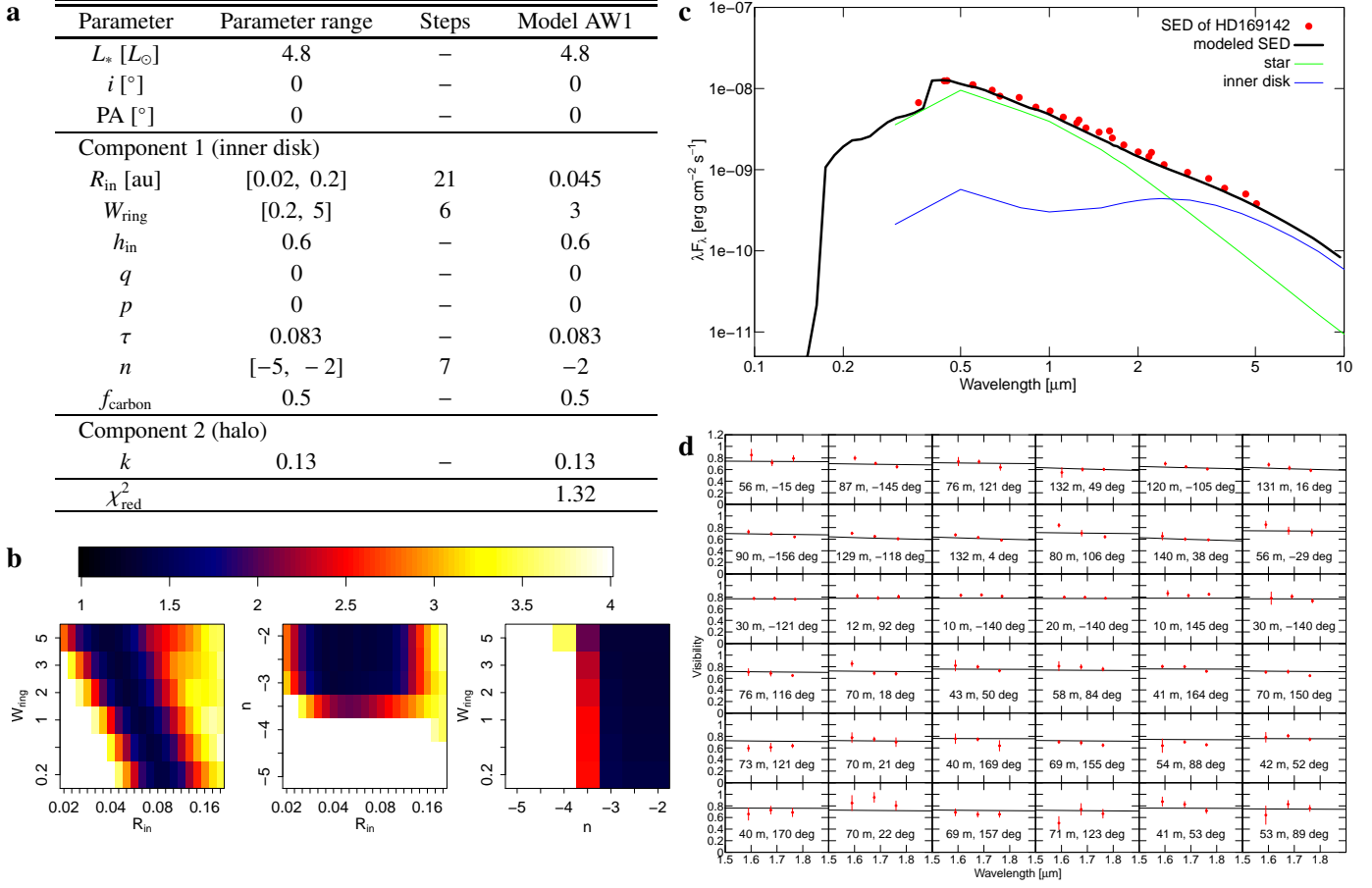


**Fig. A.2.** As Fig. 4, but for model run AW, compared with the data set. Model AW1 is the model with minimum  $\chi^2_{\text{red}}$ .

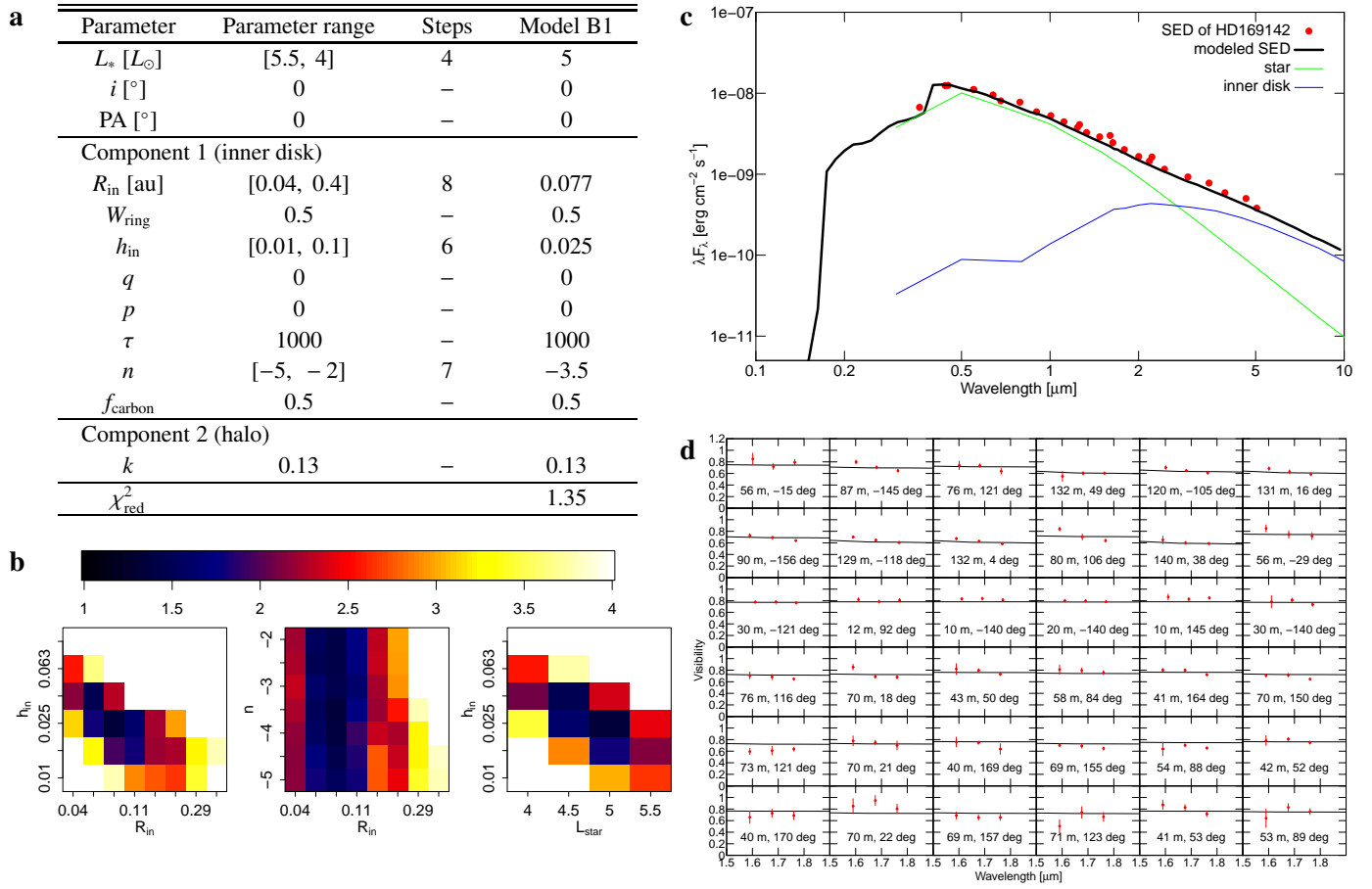


**Fig. A.3.** As Fig. 4, but for model run B, compared with the data set. Model B1 is the model with minimum  $\chi^2_{\text{red}}$ .